



HAL
open science

Ridge polariton laser: different from a semiconductor edge-emitting laser

H Souissi, M Gromovyi, T Gueye, C Brimont, L Doyennette, D D Solnyshkov, G Malpuech, E Cambril, S Bouchoule, B Alloing, et al.

► To cite this version:

H Souissi, M Gromovyi, T Gueye, C Brimont, L Doyennette, et al.. Ridge polariton laser: different from a semiconductor edge-emitting laser. 2022. hal-03521600v1

HAL Id: hal-03521600

<https://hal.science/hal-03521600v1>

Preprint submitted on 11 Jan 2022 (v1), last revised 5 Oct 2022 (v2)

HAL is a multi-disciplinary open access archive for the deposit and dissemination of scientific research documents, whether they are published or not. The documents may come from teaching and research institutions in France or abroad, or from public or private research centers.

L'archive ouverte pluridisciplinaire **HAL**, est destinée au dépôt et à la diffusion de documents scientifiques de niveau recherche, publiés ou non, émanant des établissements d'enseignement et de recherche français ou étrangers, des laboratoires publics ou privés.

Ridge polariton laser: different from a semiconductor edge-emitting laser

H. Souissi,^{1,*} M. Gromovi,^{2,3} T. Gueye,¹ C. Brimont,¹ L. Doyennette,¹ D.D Solnyshkov,^{4,5} G. Malpuech,⁴ E. Cambril,² S. Bouchoule,² B. Alloing,³ S. Rennesson,³ F. Semond,³ J. Zúñiga-Pérez,³ and T. Guillet^{1,†}

¹Laboratoire Charles Coulomb (L2C), Université de Montpellier, CNRS, Montpellier, France

²Centre de Nanosciences et de Nanotechnologies, CNRS, Université Paris-Saclay, France

³UCA, CRHEA-CNRS, Rue Bernard Gregory, 06560 Valbonne, France

⁴Université Clermont Auvergne, CNRS, Institut Pascal, Clermont-Ferrand, France

⁵Institut Universitaire de France (IUF), 75231 Paris, France

(Dated: January 11, 2022)

We experimentally demonstrate the difference between a ridge polariton laser, and a conventional edge-emitting ridge laser operating under electron-hole population inversion. The horizontal laser cavities are 20 – 60 μm long GaN etched ridge structures with vertical Bragg reflectors. We investigate the laser threshold under optical pumping and assess quantitatively the effect of a varying optically-pumped length. The laser effect is achieved for an exciton reservoir length of just 15% of the cavity length, which would not be possible in a conventional ridge laser, with an inversion-less polaritonic gain about 10 times larger than in equivalent GaN lasers. The modelling of the cavity free spectral range demonstrates the polaritonic nature of the modes.

There are two conditions required for a laser to operate. The first is population inversion for a given electronic transition, so that the emission of the electronic system at the lasing frequency overcomes absorption, which can eventually vanish if the electronic system is fully inverted. In any case, the gain of the fully inverted system cannot exceed the maximal absorption, as prescribed by the well-known Einstein relations relating the rates of absorption and stimulated emission [1, 2]. The second condition for lasing to occur is that gain overcomes the losses, essentially the decay rate of the photonic cavity constituting the laser.

Polariton lasers [3–5] are coherent emitters based on hybrid quasi-particles arising from the strong coupling between excitons and photons, so-called exciton-polaritons. They are by construction close to the so-called exciton lasers introduced in the seventies to explain laser-like emission in certain semiconductors such as ZnO [6]. Their putative advantage over conventional lasers is that they do not require population inversion, but only that the net spontaneous scattering rate from an excitonic reservoir overcomes the decay rate of the polariton mode. Following the proposal of a polariton laser without population inversion [3], the demonstration of polariton lasing [7] was initially described and discussed in terms of cavity losses and an effective polaritonic gain. The focus was later brought to a thermodynamic description in terms of polariton condensation in the ground state of a cavity polariton system [8, 9] and, ultimately, to the competition between kinetic and thermodynamic aspects of the condensation process [10–13]. One should notice that photon condensation can also be realized in large area surface emitting lasers [14], or by relaxing the population inversion condition in a molecular media with large Stokes shift between emission and absorption [15]. Back to polariton lasers, the most striking evidence of an operation regime without population inversion is the

observation of two successive lasing thresholds: polariton lasing and lasing with population inversion [16, 17].

The polariton waveguide geometry has been explored for about a decade [18–27]. In the context of the current work, it presents the advantage to allow a selective excitation of only a part of the horizontal optical cavity confining the laser mode and revisit, thereby, laser interpretative frameworks. Indeed, considering the balance between gain in the excited section and absorption, lasing achieved by pumping less than one half of an homogeneous active medium filling the cavity demonstrates a lasing mechanism not based on population inversion.

In this work we study GaN-based deep-ridge waveguides delimited by GaN/air distributed Bragg reflectors (DBRs) and supporting polariton modes (Fig. 1 and Appendix A). The 20 μm and 60 μm –long cavities display thus a design very similar to the most common ridge semiconductor lasers, including recent InGaN-based devices [28]. We observe that lasing occurs while pumping only 15% of the cavity length. It demonstrates the absence of reciprocity between gain and absorption in our system and represents a unique and very clear demonstration of the occurrence of polariton lasing.

Cavity imaging and spectroscopy - The optical investigations are performed by microphotoluminescence imaging (μPL , see Appendix B). The cavity is pumped with a pulsed laser (355 nm, 7 kHz rate, 4 ns pulses) resonantly exciting the exciton reservoir with a line-shaped spot profile (Fig. 1(b)) which length L_{pump} can be adjusted to excite partially or entirely the cavity, therefore controlling the size of the exciton reservoir. Figure 1(c) shows a spatially- and spectrally-resolved PL image of the 60 μm -long cavity collected perpendicular to the sample, and for a 6.5 μm -long pump. At the position of the excitation spot, the spectrum consists in a broad central emission associated to the excitonic reservoir and its optical phonon replicas (Fig. 1(d), black spectrum). At the posi-

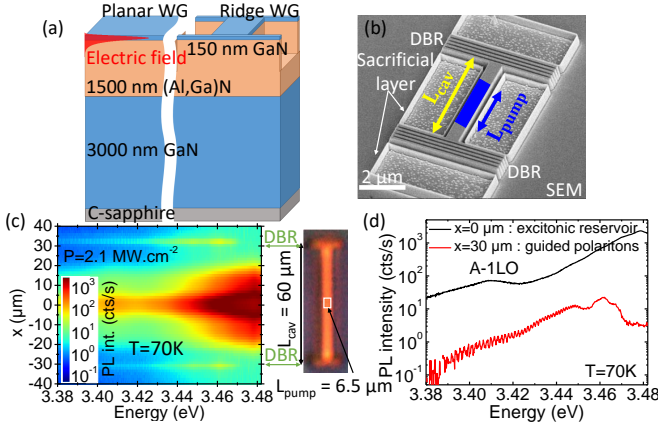


FIG. 1. Sample description. (a) Sample structure (left: planar waveguide after epitaxy, right: ridge cavity after lithography and 800 nm-deep etching; electric field intensity distribution of the fundamental mode TE₀, in red); (b) Scanning electron micrograph image of a 5 μm-long polariton ridge waveguide. The adjustable pump spot is sketched in blue; (c) μPL image and microscope image of a 60 μm-long cavity excited below lasing threshold, and a line-shaped excitation spot ($L_{pump} = 6.5 \mu\text{m}$, white rectangle); (d) Emission spectra extracted from (c) at positions 0 μm (excitation spot) and 30 μm (DBR).

tion of the DBRs acting as reflectors but also as scatterers towards the microscope objective, the specific emission is attributed to the guided polaritons ($x = \pm 30 \mu\text{m}$, red spectrum), with a series of sharp peaks corresponding to the Fabry-Perot (FP) modes of the cavity. Their free spectral range (FSR) is inversely proportional to the cavity length, as detailed below.

Laser operation - Figure 2(a) shows a series of power-dependent PL spectra recorded at the DBR position for a 20 μm-long cavity excited by a 3 μm-long pump spot positioned at the cavity center. The spectra exhibit FP modes over a large energy range. For the mode at 3.452 eV (square mark), the intensity rapidly increases by about one order of magnitude across a threshold value $P_{th} = 1.26 \text{ MW.cm}^{-2}$ of the excitation power (Fig. 2(b)). This mode also evidences a line narrowing beyond threshold, with a decrease of the full width at half maximum (FWHM) from 1.1 meV down to 0.65 meV. These two features evidence the laser operation of the device. On the contrary, for a non-lasing FP mode at negative detuning (open circle mark), the intensity undergoes a linear increase vs the pump power and the linewidth remains almost constant with a FWHM of 1.15 meV.

Polariton dispersion - In order to assess the strong coupling regime between photons and excitons, the most direct method would be to monitor the dispersion of polaritons using diffraction gratings on top of the core layer. This geometry was exploited for polariton waveguides based on GaAs [18, 23], GaN [20, 29], and ZnO [22]. It allowed measuring the lower polariton branch (LPB)

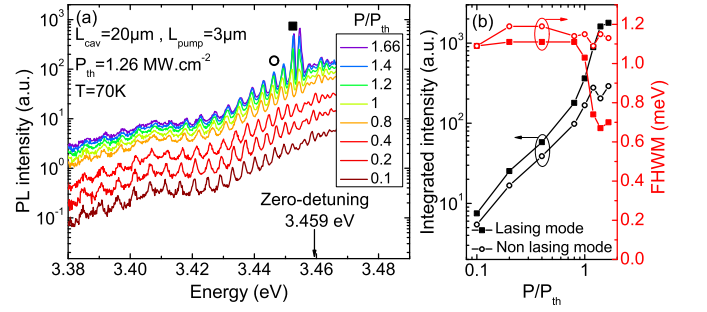


FIG. 2. Laser operation of the 20 μm-long cavity at 70K. (a) Power-dependent PL spectra across the lasing threshold; (b) intensity (black) and linewidth (red) of the lasing and the non-lasing modes.

dispersion and observing the anticrossing between lower and upper polariton branches (UPB). For laser cavities, in order to avoid the losses associated to such gratings, the polariton dispersion can be indirectly deduced from the measured cavity FSR. This method has been previously implemented in the case of ZnO-nanowires [30, 31], and ZnO polaritonic waveguides (Supplemental Material in Ref. 22). Indeed, the wavevector β_n associated to the n -th longitudinal mode is $\beta_n = n.\pi/L_{cav}$, where L_{cav} is the length of the cavity. The spectrum of FP modes below threshold allows to estimate the FSR as well as the cavity finesse, *i.e.* the total cavity losses. We therefore fit the FP transmission spectrum (Fig. 3.(a),(b), see Appendix E), an approach analogous to the Hakki-Paoli method, which provides the gain as a function of energy [32].

The Figure 3(c) compares the FSRs extracted from the FP transmission spectra, below and above threshold, to the FSRs from calculated dispersions, based on the Elliott-Tanguy susceptibility developed in Ref. 29, for the LPB and for the bare photon mode (in the absence of exciton transitions in the dielectric function). The parameters of the model (exciton energies and linewidths) are deduced from reflectivity spectra measured on the same planar waveguide structure (Fig. 5). The agreement between experimental and calculated FSR dispersions is obtained for the TE₀ mode strongly coupled to excitons, with a reduction of the oscillator strength of 30% below threshold (0.1 and 0.2 × P_{th}), and 40% above threshold ($P = 1.8 \times P_{th}$). This result demonstrates the operation in the strong coupling regime, with a slight diminution of the excitonic oscillator strength that could be related to a degradation of the structural and optical quality of the GaN active material during the deep-etching of the ridge. The zero-detuning condition ($\delta = 0$) is realized at an LPB energy of 3.459 eV, and the exciton-photon coupling strength (Rabi splitting) amounts to $\Omega_{Rabi} = 66 \pm 10 \text{ meV}$ (Fig. 6(a)). The observed lasing mode lies close to zero-detuning, corresponding to an estimated exciton fraction of 40% (Fig. 6(b)).

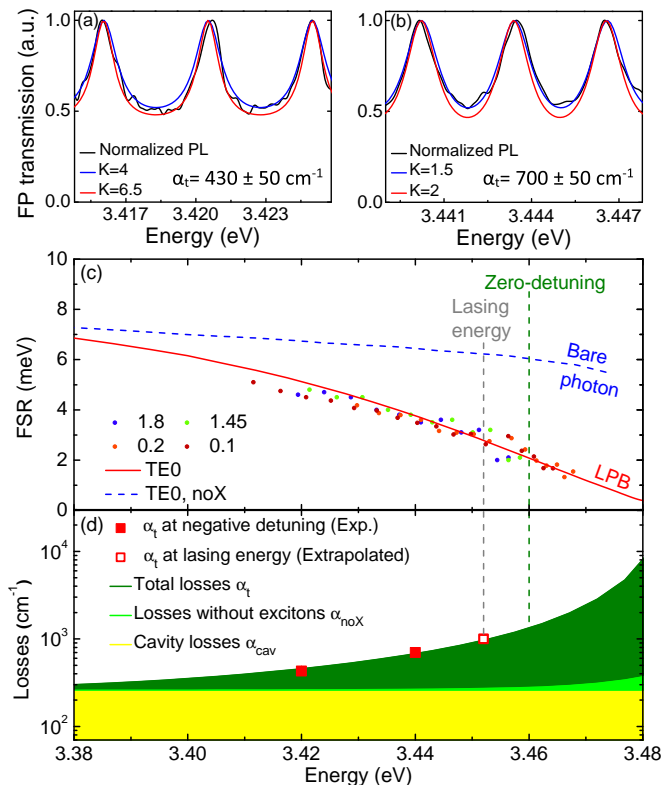


FIG. 3. Modeling of the Fabry-Perot modes of the $20 \mu\text{m}$ -long cavity at $T = 70 \text{ K}$. (a,b) Experimental estimate of the FP transmission (black line), and its fit for various coefficient of finesse K (red and blue lines); (c) Experimental FSR vs excitation power (colored dots) and FSR calculated from LPB dispersions (plain line); (d) Calculated contributions to the total losses α_t (dark green curve), from Elliott-Tanguy model, compared to experimental total losses deduced from FP transmission (red square dots). The open red square dot corresponds to the estimated total losses at the lasing energy $\alpha_t = 1000 \pm 50 \text{ cm}^{-1}$.

The polariton laser operation has been investigated as a function of sample temperature (Fig. 9). Up to $T = 150 \text{ K}$, the FP modes are observed below and above threshold, and the strong coupling can be assessed from their FSR. At $T = 220 \text{ K}$, lasing is observed but we cannot conclude on the lasing regime.

Laser losses and gain - The finesse of the FP modes strongly depends on the energy. The corresponding total cavity losses increase from $430 \pm 50 \text{ cm}^{-1}$ at 3.42 eV to $700 \pm 50 \text{ cm}^{-1}$ at 3.44 eV (Fig. 3(a,b)). They can be decomposed into three contributions:

$$\alpha_t = \alpha_{cav} + \alpha_{pol} + \alpha_{noX}.$$

The cavity losses $\alpha_{cav} = \alpha_i + \alpha_m$ include the internal losses α_i and the mirror losses $\alpha_m = \frac{-\ln R_{DBR}}{L_{cav}}$ resulting from the finite DBR reflectivity R_{DBR} . The losses without excitons α_{noX} and the polariton losses α_{pol} are deduced from the simulations based on the Elliott-Tanguy susceptibility [29]. The three contributions are repre-

sented in Figure 3(d). The cavity losses $\alpha_{cav} = 250 \text{ cm}^{-1}$ provide a significant contribution to the total losses only at large negative detunings.

Above 3.45 eV , the intrinsic contribution of polariton losses α_{pol} increases and degrades the cavity finesse, which cannot be experimentally determined. However, the good quantitative agreement between experimental and simulated total losses at negative detuning (red square dots and dark green curve in Fig. 3(d)) allows estimating the total losses at the lasing energy of about $1000 \pm 100 \text{ cm}^{-1}$.

Dependence on the pump length - To further understand the polariton laser dynamics, and compare with conventional edge-emitting semiconductor lasers, we study the effect of the pump length versus the cavity length, in analogy with the segmented contact method for electrically injected ridge lasers [33], or the variable stripe-length method for gain measurement [34]. The gain is fed by the exciton reservoir in a polariton laser, so that the gain length can be estimated from the spatial profile of the exciton reservoir (Fig. 8). The measured size of the exciton reservoir is slightly larger than the length of the excitation spot, which is a signature of a $1 - 3 \mu\text{m}$ spatial diffusion of the excitons independent of the excitation power in the investigated power range.

The dependence of the spatially integrated laser power at threshold ($p_{th}^{(i)}$) versus the gain length L_{gain} (Fig. 4(a)) presents similar scaling laws for the $L_{cav} = 20 \mu\text{m}$ and $60 \mu\text{m}$. The laser effect is achieved even for a pump length of just 10% of the cavity (corresponding to a reservoir length of 15% of the cavity), with only a threefold increase of the overall threshold.

Model of the polariton laser kinetics - In order to compare our experimental results with a kinetic model, we simulate the polariton relaxation in the waveguide structure with mirrors using the semiclassical Boltzmann equations for exciton-polaritons [4, 35] combining real and reciprocal space resolution [19, 27]. The results of this kinetic model are shown in Figure 4(a). A good quantitative agreement between experimental results and simulations is obtained, confirming a striking consequence of polariton lasing: threshold can be reached even when pumping just one tenth of the cavity length.

Model of the gain versus pump length - In a conventional ridge laser, lasing action appears due to the reciprocity between absorption and stimulated emission, and requires to achieve a population inversion in the electron and hole bands: the maximum gain (γ_{e-h}) at a given energy is smaller than the corresponding absorption (α_0) at zero carrier density [36]. In a segmented laser with a gain section smaller than the full cavity, the gain and loss terms in both pumped and unpumped sections are compared in Table I, and the threshold condition writes:

$$e^{-2(\alpha_m + \alpha_i)L_{cav}} \cdot e^{-2\alpha_0(L_{cav} - L_{gain})} \cdot e^{2\gamma_{e-h,th}L_{gain}} = 1,$$

where $\gamma_{e-h,th}$ is the electron-hole modal gain at thresh-

TABLE I. Losses/gain in each cavity section for a conventional edge-emitting laser and a polariton laser. γ_{e-h} and γ_{pol} are the electron-hole gain and the polariton gain, respectively. The cavity losses are the sum of the mirror losses α_m and the internal losses α_i . α_{pol} and α_{noX} are the polariton losses and the losses without excitons, respectively.

Laser	Gain section L_{gain}	Unpumped section $L_{cav} - L_{gain}$	Full cavity L_{cav}
Conventional laser	$+\gamma_{e-h} (< \alpha_0)$	$-\alpha_0$	$-\alpha_m - \alpha_i$
Polariton laser	$+\gamma_{pol} - \alpha_{pol} - \alpha_{noX}$	$-\alpha_{pol} - \alpha_{noX}$	$-\alpha_m - \alpha_i$

old. Assuming $\gamma_{e-h,th} = \alpha_0$, *i.e.* in the $T = 0$ limit, we have:

$$\gamma_{e-h,th} = \frac{(\alpha_m + \alpha_i) \cdot L_{cav}}{2L_{gain} - L_{cav}} = \frac{\alpha_{cav} \cdot L_{cav}}{2L_{gain} - L_{cav}} \quad (1)$$

Lasing action in a conventional ridge laser is obtained if more than half of the cavity is excited (Fig. 4(b), dash dotted line).

In the case of a polariton laser, the polariton losses α_{pol} and the losses without excitons α_{noX} are expected in the whole cavity, *i.e.* even in the gain section. Moreover, the gain originates from the stimulated relaxation from the pumped exciton reservoir to the lasing polariton mode, illustrating that the polariton gain and the polariton losses are not correlated. The condition of laser oscillations at threshold writes:

$$e^{-2(\alpha_m + \alpha_i) \cdot L_{cav}} \cdot e^{-2(\alpha_{noX} + \alpha_{pol}) \cdot L_{cav}} \cdot e^{2\gamma_{pol,th} \cdot L_{gain}} = 1,$$

which leads to the expression of the polariton gain at

threshold:

$$\gamma_{pol,th} = \frac{(\alpha_m + \alpha_i + \alpha_{noX} + \alpha_{pol}) \cdot L_{cav}}{L_{gain}} = \frac{\alpha_t \cdot L_{cav}}{L_{gain}} \quad (2)$$

Equation (2) allows estimating the polariton gain from the previous analysis of the cavity losses. The modelled total losses α_t have been validated at negative detuning from the analysis of the finesse of the FP cavity, and then extrapolated to the lasing energy. At threshold, the deduced modal gain is shown on the Figure 4(b) (plain line) as a function of the gain length. For a realistic comparison of the polariton and conventional lasing schemes, only the cavity losses are considered for the conventional ridge lasers (indicated in yellow), the gain being of the same order of magnitude of the one measured for analogous nitride ridge lasers [28]. Instead, both cavity and polariton losses (indicated in green) are considered in the case of the polariton laser. Our analysis explains why a polariton laser does not require at least half of the cavity to be pumped, and provides a clear experimental evidence of this striking feature specific to polariton lasers.

Finally, the dependence of the polariton gain versus the experimental laser threshold (P_{th}) is shown in the Figure 4(c), based on the experimental data for both $L_{cav} = 20 \mu m$ and $60 \mu m$: the two corresponding gain curves are superimposed. It is worth noting that a record modal gain of $6600 cm^{-1}$ is reached for a short pump length (1000 cm^{-1}). In an early GaN laser diode, a modal gain of about $400 - 600 cm^{-1}$ was initially deduced from experiments [37]. More recently, in order to reach a laser operation in short cavities ($L_{cav} = 45 - 280 \mu m$) with high-reflectivity dielectric DBRs, a modal gain less than $100 cm^{-1}$ has been extracted [28]. The polariton laser therefore provides a strong increase of the gain for comparable geometry and length.

Conclusion - We have studied laser cavities in GaN etched ridge structures with DBRs. A laser threshold of the order of few hundreds of $kW.cm^{-1}$ is reached, with a large gain allowing for shorter cavities compared to standard ridge GaN lasers. Beyond the demonstration of lasing, we have assessed the robustness of the strong coupling regime by comparing the cavity FSR to polariton dispersions based on the Elliott-Tanguy model [29]. We

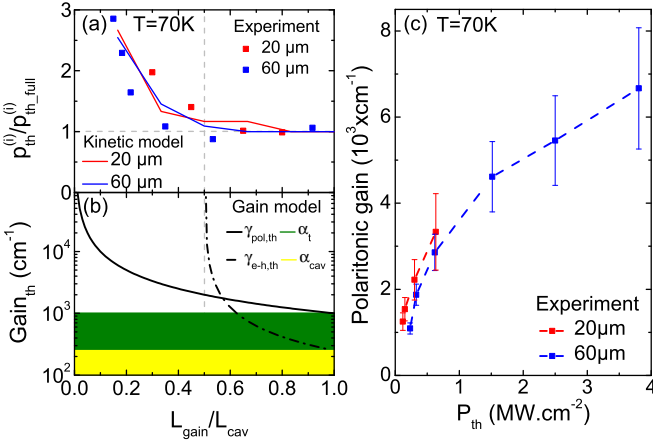


FIG. 4. Polariton laser vs. conventional semiconductor laser. (a) Laser power at threshold $p_{th}^{(i)}$, integrated along the whole excitation length, vs gain length, normalized to its value $p_{th,full}^{(i)}$ for $L_{pump} = L_{cav}$. The $p_{th,full}^{(i)}$ are respectively 77 and 480 $pJ/pulse$ for cavities lengths $20 \mu m$ and $60 \mu m$; (b) Modal gain at threshold calculated vs gain length. Plain line: case of polariton laser (Eq. (2)). Dash dotted line: conventional semiconductor laser (Eq. (1)). (c) Calculated modal gain at threshold vs experimental power density at laser threshold P_{th} . Here, the dashed line is a guide for the eyes.

demonstrate polariton laser operation up to 150 K. Most important, we experimentally demonstrated how a ridge polariton laser is different from a standard ridge laser. By monitoring the threshold as a function of the optical pumping length, *i.e.* the size of the exciton reservoir, we illustrate that a polariton laser can operate with a reservoir (*i.e.* a gain region) covering only 15% of the full cavity, versus a theoretical lower bound of 50% for the pump length of a conventional laser. This experimental observation agrees quantitatively with simulations based on semiclassical Boltzmann equations for polaritons.

ACKNOWLEDGEMENTS

The authors acknowledge fundings from the French National Research Agency (ANR-24-CE24-0021-03, ANR-11-LABX-0014), the French Renatech network and the Region Occitanie (ALDOCT-001065).

APPENDIX A - SAMPLE FABRICATION

The sample consists in a GaN waveguide (WG) grown by metal-organic vapor phase epitaxy (MOVPE) on *c*-plane sapphire. The structure is detailed in Figure 1(a). It consists in a 3000-nm-thick GaN buffer, a 1500-nm-thick $Al_{0.08}Ga_{0.92}N$ cladding and a 150-nm-thick GaN waveguide core. The spatial profile of the zeroth-order transverse electric mode (TE0) (Fig.1(a), red line) shows that the waveguide is almost monomode regarding the vertical confinement, with a confinement factor of 76%.

From the planar slab waveguide, ridge waveguides with GaN/air DBRs have been defined by electron beam lithography and dry deep etching in order to benefit simultaneously of lateral optical confinement and efficient mirrors. Figures 1(a) and 1(b) present the sample scheme and the scanning electron microscope (SEM) image of full in-plane cavity, including the ridge and the 4-pair Bragg mirrors. The cavities have a 1 μm ridge width, 4-pair DBRs and a cavity length L_{cav} varying from 5 to 60 μm . A complementary focused ion beam etching is performed, which improves the sidewall verticality of the ridge and mirrors and leads to the presence of a sacrificial vertical layer all around the structure. This sacrificial layer, visible on the SEM picture (Fig.1(b)), does not affect the optical modes. In this work, we will focus on two devices with cavity lengths 20 μm and 60 μm .

APPENDIX B - EXPERIMENTAL SETUP

Under a flow of liquid nitrogen, the sample is mounted in a cryostat with a temperature controller adjustable between 70 and 300 K. The sample is excited using a pulsed laser source at 355 nm, emitting a pulse-width

of 4 ns with a repetition rate of 7 kHz (Cobolt Tor). The laser power reaching the sample is controlled with a half-wave plate and a polarizer, together with optical densities. An line-shaped spot is obtained by inserting a variable slit and a cylindrical lens between the beam expander and the microscope objective. The spot width matches the ridge width. The slit is used to manually adjust the spot length L_{pump} . The microscope objective (20x) focuses the pump beam on the sample, and collects the emitted signal from the cavity. The cavity is imaged onto the spectrometers input slit. A Charge Coupled Device (CCD) coupled to the 55 cm-long spectrometer (Horiba Jobin Yvon iHR550), with a diffractive grating with 1200 lines per mm, allows to reconstruct the real space image.

APPENDIX C - EXCITON ENERGIES AND BROADENINGS

The A and B excitons energies are deduced from reflectivity experiments performed on unprocessed regions of the same sample. This leads to A and B excitons at 3.492 eV and 3.5 eV, respectively (Fig. 5(a)). The fit of the reflectivity provides an estimate of the homogeneous and inhomogeneous broadenings ($\gamma = 1$ meV, $\sigma = 2$ meV).

The PL spectra of the 20 μm -long cavity, versus pump-

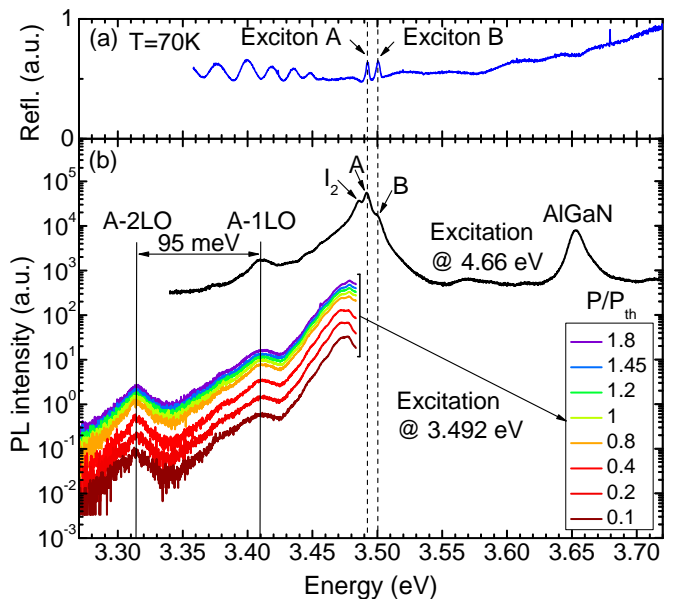


FIG. 5. Low temperature measurements. (a) Reflectivity performed on the same sample. (b) Emission spectra at $T = 70$ K under non-resonant excitation at 4.66 eV (*i.e.* 266 nm laser, black line) and under quasi-resonant excitation at 3.492 eV vs. pump power (*i.e.* 355 nm laser, colored lines). The emission is measured at the position of the excitonic reservoir ($x = 0$ μm) of a 20 μm -long cavity.

ing power, measured at 70 K under the pump spot ($L_{pump} = 6.5 \mu\text{m}$, $x = 0 \mu\text{m}$: excitonic reservoir), is shown in Figure 5(b). These spectra are compared to the PL spectrum under pulsed non-resonant excitation at 266 nm (4.66 eV) (Fig. 5(b), black line). We observe the A and B excitons, as well as the neutral donor bound recombination (I2 line)[38]. The peak at 3.652 eV corresponds to the AlGaIn cladding layer. The longitudinal-optical phonon replicas, 1LO and 2LO, of the exciton emission are observed at 3.409 and 3.314 eV, respectively. Let us emphasize that the zero-phonon emission of the reservoir is at the energy of the quasi-resonant excitation laser, so that we cannot measure it in our experiments. However the LO-phonon replicas can be easily analyzed, with constant line-shape and energy, across the whole range of excitation power. This proves that the exciton energy remains stable at all investigated powers.

APPENDIX D - MODELING THE POLARITON DISPERSION

In order to determine the exciton-photon coupling strength, the coupled oscillator model is the simplest and most widely used, but it largely overestimates the coupling strength for waveguide polaritons. In a previous work[29], we proposed a more accurate model that takes into account the dielectric susceptibility near the excitonic transition. The corresponding polariton dispersions (LPB) are presented in Figure 6(a), together with the dispersion of the bare guided mode, in the absence of exciton transitions in the dielectric function. Quantitatively, the two models lead to a zero-detuning condition ($\delta = 0$) spectrally shifted with respect to each other, giving, in turn, very different estimations of the actual Rabi

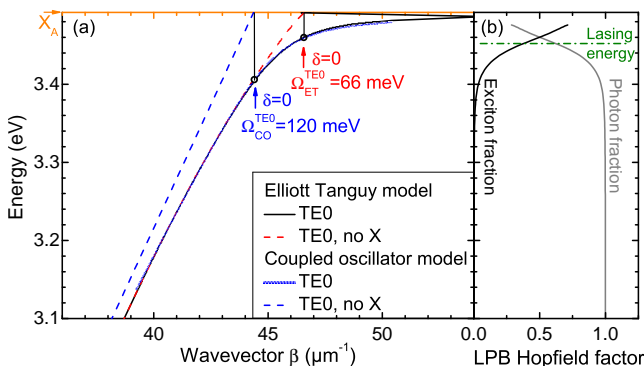


FIG. 6. (a) Coupled oscillator modeling of the TE0 (blue) versus the Elliott-Tanguy model of the TE0 (red) of the polaritons dispersions. The corresponding bare waveguide modes are indicated as dashed lines, and the A exciton energy as a horizontal blue line. The vertical black lines indicate the zero-detuning condition for each model, and the associated Rabi splitting. (b) Hopfield coefficients of the LPB, for the Elliott-Tanguy model.

splitting: 120 meV for the coupled oscillator model and 66 meV for the Elliott-Tanguy model, corresponding to a zero-detuning condition at an LPB energy of 3.459 eV. All comparison of FSR dispersions with simulated dispersions are obtained within the Elliott-Tanguy model, and the material parameters are fixed as detailed in the section “Exciton energies and Broadenings”. The excitonic and photonic fractions of the LPB are presented in Figure 6(b), showing that the LPB is 40% excitonic at the lasing energy.

APPENDIX E - QUANTIFYING THE FSR AND LOSSES OF FABRY-PEROT MODES

Qualifying the Fabry-Perot cavity is an important step to assess the strong coupling regime and the value of the total losses α_t from the coefficient of finesse K . The Fabry-Perot transmission is obtained by normalizing the PL spectrum to its envelope. Due to our collection scheme (perpendicular to the waveguide plane), the very strong spontaneous emission of the exciton reservoir under the excitation spot also contributes to the signal collected at the DBRs, even if far apart. The FP transmission can be fitted by the expression:

$$T_{FP}(\lambda) = C + (1 - C) \cdot \frac{1}{1 + K \cdot \sin^2(2\pi \cdot n_g(\lambda) \cdot \frac{L_{cav}}{\lambda} + \varphi_0)} \quad (3)$$

where $n_g(\lambda) = \frac{v_g}{c}$ is the group index, v_g is the group velocity, φ_0 is the adjustment phase, and C corresponds to the background PL of the exciton reservoir. This led to estimate the coefficient of finesse K (Fig. 3(a) and 3(b) of the main text), and thus the finesse \mathcal{F} .

$$K = \frac{4e^{-\alpha_t \cdot L_{cav}}}{[1 - e^{-\alpha_t \cdot L_{cav}}]^2} \quad (4)$$

$$\mathcal{F} = \frac{\Delta\lambda}{\lambda} = \frac{\pi}{2 \cdot \arcsin(\frac{1}{\sqrt{K}})} \quad (5)$$

From the coefficient of finesse K , we can therefore deduce the total losses α_t . As discussed in the letter, the total losses at large negative detuning are attributed to the cavity losses, $\alpha_{cav} = 250 \text{ cm}^{-1}$. They are the sum of internal losses (absorption by defects, roughness-induced losses) and the mirror losses. We can estimate a lower bound of the DBR reflectivity $R_{DBR} = 0.6$ if we neglect internal losses and therefore attribute all cavity losses to the mirrors.

Above 3.45 eV, the intrinsic contribution of polariton losses degrades the cavity finesse (Fig. 2(a)), so that the FP transmission exhibits almost sinusoidal oscillations. This prevents a proper fit of their lineshape, so that the finesse cannot be experimentally determined.

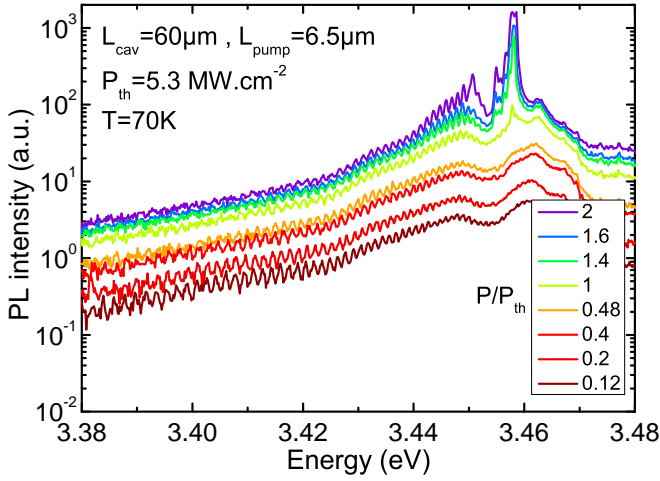


FIG. 7. Study of the cavity $60 \mu\text{m}$. Emission at 70 K versus pumping power. The $60 \mu\text{m}$ length cavity is excited by a $6.5 \mu\text{m}$ sized-pump.

APPENDIX F - CAVITY-LENGTH DEPENDENCE OF THE FSR

The series of PL spectra measured at 70 K of a $60 \mu\text{m}$ -long cavity as a function of pumping power, for an excitation wavelength of 355 nm ($L_{\text{pump}} = 6.5 \mu\text{m}$) are presented in Figure 7. One can see also Fabry-Perot modes spreading over a large energy range, with a free spectral range (FSR) three times smaller than that of the $20 \mu\text{m}$ long cavity. This is due to the fact that the FSR is inversely proportional to the cavity length.

APPENDIX G - EXCITON DIFFUSION

Let us now study the effect of the pump length (L_{pump}) on the size of the excitonic reservoir (L_{gain}). Figure 8(a) shows the spatial profile of the laser at different openings of the variable slit. The FWHM allows us to estimate L_{pump} . In the case of polariton laser, the physical origin of the gain is the stimulated relaxation from the pumped exciton reservoir to the lasing polariton mode. Since the energy of the pump laser is resonant with the exciton energy, we prefer estimating the gain length (L_{gain}) from the spatial profiles of the longitudinal-optical phonon replicas (1LO or 2LO) and their FWHM (Fig. 8(b)). The result of the comparison between L_{gain} and L_{pump} is shown in Figure 8(c). The exciton reservoir (L_{gain}) is slightly larger than the length of the excitation spot (L_{pump}), due to the spatial diffusion of the excitons which is of the order of $1 - 3 \mu\text{m}$.

APPENDIX H - EFFECT OF TEMPERATURE

The polariton laser operation has been investigated as a function of sample temperature. The power dependent emission spectra measured at 150 K on the $20 \mu\text{m}$ -long cavity with a $6.5 \mu\text{m}$ sized-pump is shown in Figure 9(a). Similarly to the $T = 70 \text{ K}$ case, the Fabry-Perot modes are observed for a large energy range below threshold. The calculated FSR of the guided modes was again extracted from the dispersions based on the Elliott-Tanguy model of the dielectric susceptibility, as shown as plain lines in Figure 9(b). The experimental

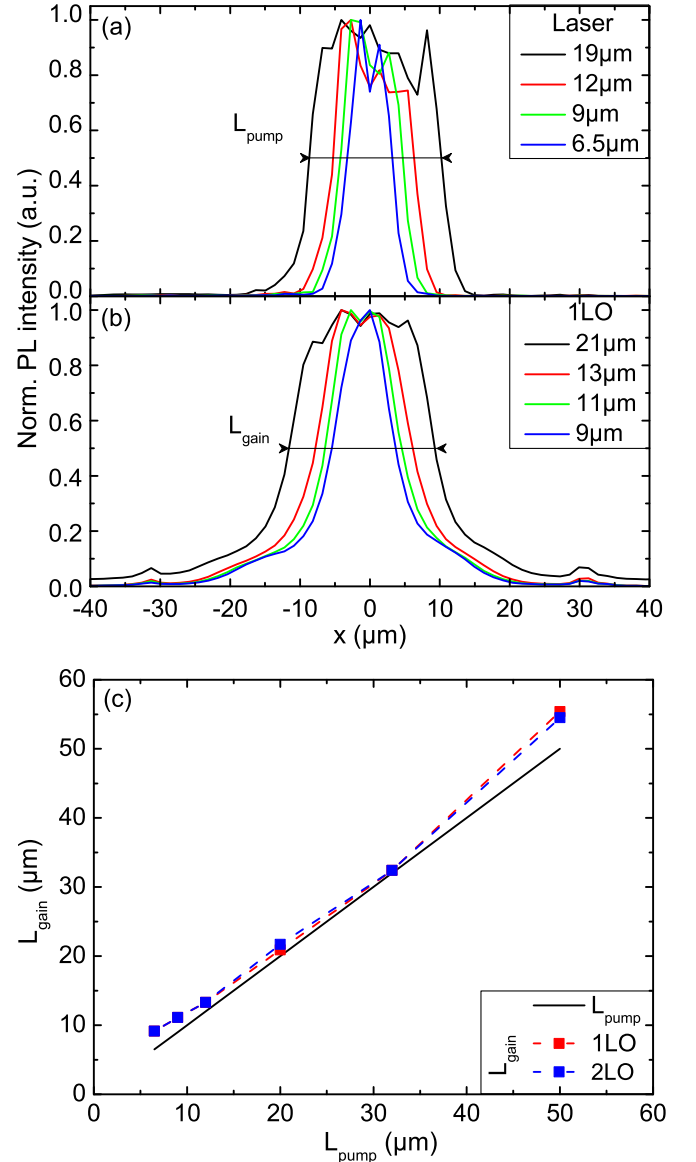


FIG. 8. (a) The spatial profile of the laser spot for different slit opening. (b) Same as (a) but at the 1LO energy range. L_{pump} and L_{gain} are deduced from the FWHM. (c) Comparison of the gain length L_{gain} (1LO and 2LO) and the pump length L_{pump} .

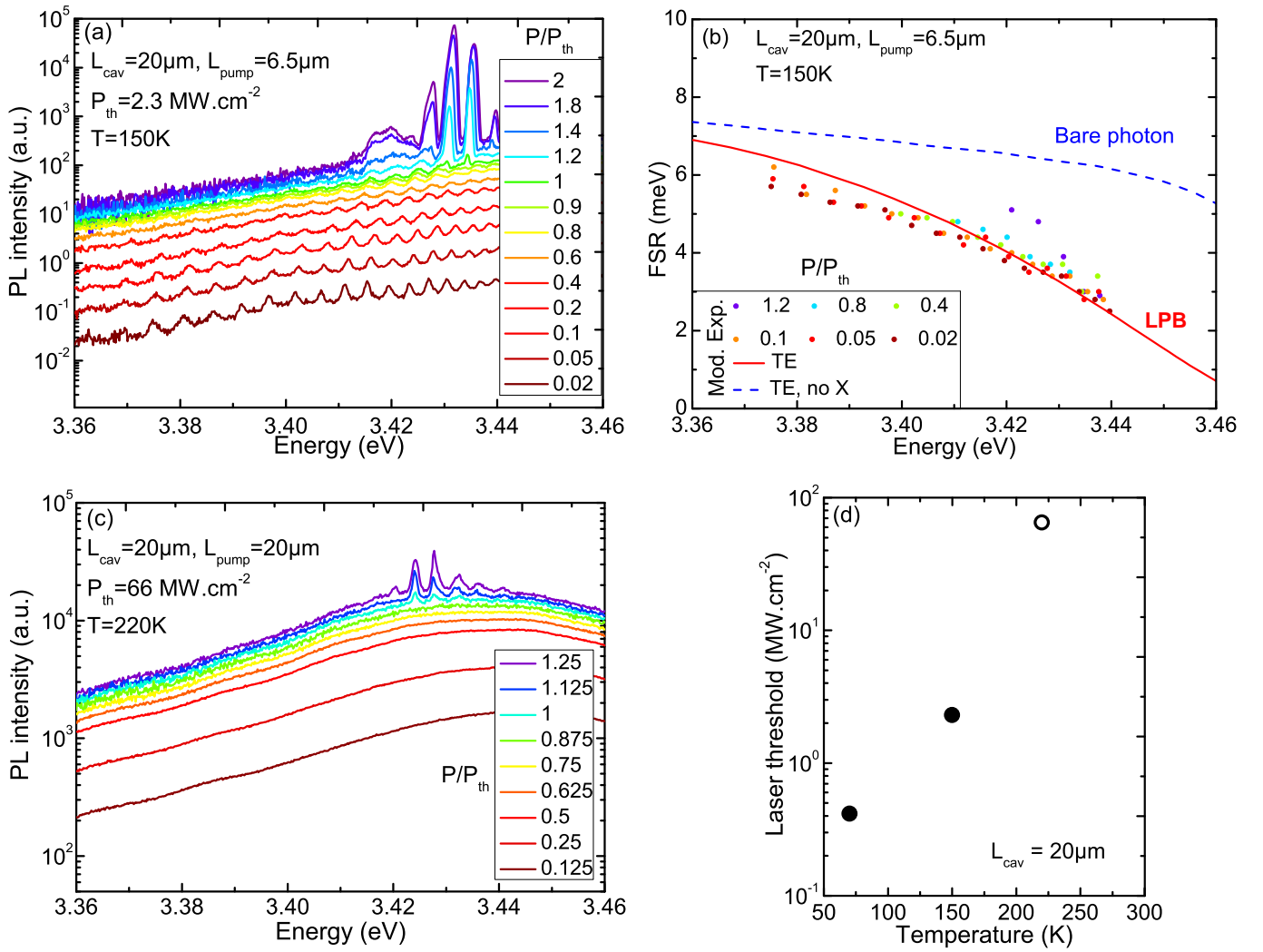


FIG. 9. Study of the 20 μm -long cavity vs. Temperature. (a) Emission at 150 K vs. pumping power. The 20 μm length cavity is excited by a 6.5 μm sized-pump; (b) Calculated FSR (plain lines) from dispersions for different oscillator strengths, and compared to measured Fabry-Perot modes (dots); (c) Emission at 220 K vs. pumping power. The cavity 20 μm is excited by a 20 μm sized-pump; (d) Temperature dependence of the laser threshold for the 20 μm length cavity. The strong coupling is verified below $T = 150\text{ K}$ (black circles) whereas it is not assessed at $T = 220\text{ K}$ (open black circle).

measurements (colored dots in Fig. 9(b)) agree with the calculated FSRs. Above threshold a small decrease of the oscillator strength of the A, B excitons has been observed, from -20% below threshold to -45% above threshold. The PL spectra of the same cavity excited by a 20 μm sized-pump for a pumping power varying from 0.125 to $1.25 \times P_{\text{th}}$ at 220 K is presented in Figure 9(c). One can see that below threshold the Fabry-Perot modes do not appear, preventing the proper demonstration of the strong coupling at this high temperature. Still, the laser effect is maintained. The temperature increase has two notorious effects: the first impact is to shift the optimum detuning (*i.e.* that for which the relaxation rate is maximum) towards more and more negative values; this can be easily understood, since at higher temperatures polaritons thermalize more efficiently along the LPB and

are thus able to reach more negative detunings. The second and most important effect is that the laser threshold displays a large increase with temperature, presently preventing CW lasing action up to 300 K, as shown in Figure 9(d).

APPENDIX I - SEMICLASSICAL MODEL OF THE POLARITON LASER KINETICS

The polariton relaxation in the waveguide cavity is simulated using the semiclassical Boltzmann equations for exciton-polaritons [4, 35] combining real and recipro-

cal space resolution [19, 27]. The equations read:

$$\begin{aligned} \frac{\partial n_{k,r}}{\partial t} = & P_{k,r} - \Gamma_k n_{k,r} - n_{k,r} \sum_{k'} W_{k \rightarrow k',r} (n_{k',r} + 1) \\ & + (n_{k,r} + 1) \sum_{k'} W_{k' \rightarrow k,r} n_{k',r} - \vartheta_g(k) \frac{\partial n_{k,r}}{\partial r} \quad (6) \end{aligned}$$

Here, $n_{k,r}$ is the polariton (or purely exciton for large wave vectors) distribution function within a cell defined by k in reciprocal space and r in real space. The real space simulation is restricted to 1 dimension, whereas in reciprocal space an isotropic distribution function is accounted for (at large wave vectors, because the excitons are not quantized), and includes the DBRs. The decay rate Γ_k accounts for both the radiative and non-radiative decay rates. The decay of polaritons through the mirrors affects the spatial propagation terms at the boundaries of the system. The pumping term $P_{k,r}$ is characterized by the size of the pumping spot in real space, whereas in reciprocal space it creates a thermalized distribution of excitons within the reservoir due to the relatively rapid formation of excitons from the injected electron-hole pairs. The scattering rates $W_{k \rightarrow k',r}$ account for both exciton-exciton and exciton-phonon scattering mechanisms. They depend on the full distribution function within each spatial cell and have to be recalculated during the relaxation (for their exciton-exciton part), to account for the change of the distribution function. The term with the group velocity ϑ_g describes the polariton propagation between adjacent spatial cells.

* Hassen.Souissi@umontpellier.fr

† Thierry.Guillet@umontpellier.fr

- [1] D. E. McCumber, “Einstein relations connecting broadband emission and absorption spectra,” *Phys. Rev.* **136**, A954–A957 (1964).
- [2] W. van Roosbroeck and W. Shockley, “Photon-radiative recombination of electrons and holes in germanium,” *Phys. Rev.* **94**, 1558–1560 (1954).
- [3] A. Imamoglu, R. J. Ram, S. Pau, and Y. Yamamoto, “Nonequilibrium condensates and lasers without inversion: Exciton-polariton lasers,” *Physical Review A* **53**, 4250–4253 (1996).
- [4] A. Kavokin and G. Malpuech, *Cavity polaritons* (Elsevier, Amsterdam, The Netherlands, 2003).
- [5] A. Kavokin, J. Baumberg, G. Malpuech, and F. Laussy, *Microcavities*, 2nd ed. (Oxford University Press, 2017).
- [6] H. Haug and K. Grob, “Exciton laser theory,” *Physics Letters A* **26**, 41–42 (1967).
- [7] L. S. Dang, D. Heger, R. André, F. Boeuf, and R. Romestain, “Stimulation of Polariton Photoluminescence in Semiconductor Microcavity,” *Phys. Rev. Lett.* **81**, 3920–(1998).
- [8] J. Kasprzak, M. Richard, S. Kundermann, A. Baas, P. Jeambrun, J. M. J. Keeling, F. M. Marchetti, M. H. Szymanska, R. André, J. L. Staehli, V. Savona, P. B. Littlewood, B. Deveaud, and Le Si Dang, “Bose-Einstein condensation of exciton polaritons,” *Nature* **443**, 409–414 (2006).
- [9] J. Kasprzak, D. D. Solnyshkov, R. André, Le Si Dang, and G. Malpuech, “Formation of an Exciton Polariton Condensate: Thermodynamic versus Kinetic Regimes,” *Phys. Rev. Lett.* **101**, 146404–4 (2008).
- [10] B. Nelsen, R. Balili, D. W. Snoke, L. Pfeiffer, and K. West, “Lasing and polariton condensation: Two distinct transitions in GaAs microcavities with stress traps,” *J. Appl. Phys.* **105**, 122414–5 (2009).
- [11] F. Li, L. Orosz, O. Kamoun, S. Bouchoule, C. Brimont, P. Disseix, T. Guillet, X. Lafosse, M. Leroux, J. Leymarie, M. Mexis, M. Mihailovic, G. Patriarche, F. Réveret, D. Solnyshkov, J. Zúñiga Pérez, and G. Malpuech, “From Excitonic to Photonic Polariton Condensate in a ZnO-Based Microcavity,” *Phys. Rev. Lett.* **110**, 196406– (2013).
- [12] O. Jamadi, F. Réveret, E. Mallet, P. Disseix, F. Médard, M. Mihailovic, D. Solnyshkov, G. Malpuech, J. Leymarie, X. Lafosse, S. Bouchoule, F. Li, M. Leroux, F. Semond, and J. Zuniga-Perez, “Polariton condensation phase diagram in wide-band-gap planar microcavities: GaN versus ZnO,” *Physical Review B* **93**, 115205 (2016).
- [13] Y. Sun, P. Wen, Y. Yoon, G. Liu, M. Steger, L. N. Pfeiffer, K. West, D. W. Snoke, and K. A. Nelson, “Bose-Einstein Condensation of Long-Lifetime Polaritons in Thermal Equilibrium,” *Physical Review Letters* **118**, 016602 (2017).
- [14] S. Barland, P. Azam, G. L. Lippi, R. A. Nyman, and R. Kaiser, “Photon thermalization and a condensation phase transition in an electrically pumped semiconductor microresonator,” *Opt. Express* **29**, 8368–8375 (2021).
- [15] J. Klaers, J. Schmitt, F. Vewinger, and M. Weitz, “Bose-Einstein condensation of photons in an optical microcavity,” *Nature* **468**, 545–548 (2010).
- [16] D. Bajoni, P. Sénellart, E. Wertz, I. Sagnes, A. Miard, A. Lemaitre, and J. Bloch, “Polariton Laser Using Single Micropillar GaAs-GaAlAs Semiconductor Cavities,” *Phys. Rev. Lett.* **100**, 047401– (2008).
- [17] D. Bajoni, “Polariton lasers. Hybrid light-matter lasers without inversion,” *Journal of Physics D: Applied Physics* **45**, 313001 (2012).
- [18] P. M. Walker, L. Tinkler, M. Durska, D. M. Whittaker, I. J. Luxmoore, B. Royall, D. N. Krizhanovskii, M. S. Skolnick, I. Farrer, and D. A. Ritchie, “Exciton polaritons in semiconductor waveguides,” *Applied Physics Letters* **102**, 012109 (2013).
- [19] D. D. Solnyshkov, H. Teras, and G. Malpuech, “Optical amplifier based on guided polaritons in GaN and ZnO,” *Applied Physics Letters* **105**, 231102 (2014).
- [20] J. Ciers, J.G. Roch, J.F. Carlin, G. Jacopin, R. Butté, and N. Grandjean, “Propagating Polaritons in III-Nitride Slab Waveguides,” *Physical Review Applied* **7**, 034019 (2017).
- [21] P. M. Walker, L. Tinkler, D. V. Skryabin, A. Yulin, B. Royall, I. Farrer, D. A. Ritchie, M. S. Skolnick, and D. N. Krizhanovskii, “Ultra-low-power hybrid light-matter solitons,” *Nature Communications* **6**, 8317 (2015).
- [22] O. Jamadi, F. Reveret, P. Disseix, F. Medard, J. Leymarie, A. Moreau, D. Solnyshkov, C. Deparis, M. Leroux, E. Cambriil, S. Bouchoule, J. Zuniga-Perez, and G. Malpuech, “Edge-emitting polariton laser and amplifier based on a ZnO waveguide,” *Light: Science & Appli-*

- cations **7**, 82 (2018).
- [23] D. G. Suárez-Forero, F. Riminucci, V. Ardizzzone, M. De Giorgi, L. Dominici, F. Todisco, G. Lerario, L. N. Pfeiffer, G. Gigli, D. Ballarini, and D. Sanvitto, “Electrically controlled waveguide polariton laser,” *Optica* **7**, 1579–1586 (2020).
- [24] P. M. Walker, C. E. Whittaker, D. V. Skryabin, E. Cancellieri, B. Royall, M. Sich, I. Farrer, D. A. Ritchie, M. S. Skolnick, and D. N. Krizhanovskii, “Spatiotemporal continuum generation in polariton waveguides,” *Light: Science & Applications* **8**, 6 (2019).
- [25] O. Jamadi, F. Réveret, D. Solnyshkov, P. Disseix, J. Leymarie, L. Mallet-Dida, C. Brimont, T. Guillet, X. Lafosse, S. Bouchoule, F. Semond, M. Leroux, J. Zuniga-Perez, and G. Malpuech, “Competition between horizontal and vertical polariton lasing in planar microcavities,” *Physical Review B* **99**, 085304 (2019).
- [26] D. M. Di Paola, P. M. Walker, R. P. A. Emmanuele, A. V. Yulin, J. Ciers, Z. Zaidi, J. F. Carlin, N. Grandjean, I. Shelykh, M. S. Skolnick, R. Butt, and D. N. Krizhanovskii, “Ultrafast-nonlinear ultraviolet pulse modulation in an alingan polariton waveguide operating up to room temperature,” 2009.02059v1.
- [27] J. Ciers, D. D. Solnyshkov, G. Callsen, Y. Kuang, J.-F. Carlin, G. Malpuech, R. Butté, and N. Grandjean, “Polariton relaxation and polariton nonlinearities in non-resonantly cw-pumped iii-nitride slab waveguides,” *Phys. Rev. B* **102**, 155304 (2020).
- [28] H. Zhang, C. W. Shih, D. Martin, A. Caut, J. F. Carlin, R. Butté, and N. Grandjean, “Short cavity InGaN-based laser diodes with cavity length below 300 μm ,” *Semiconductor Science and Technology* **34**, 085005 (2019).
- [29] C. Brimont, L. Doyennette, G. Kreyder, F. Réveret, P. Disseix, F. Médard, J. Leymarie, E. Cambril, S. Bouchoule, M. Gromovyi, B. Alloing, S. Rennesson, F. Semond, J. Zúñiga Pérez, and T. Guillet, “Strong coupling of exciton-polaritons in a bulk GaN planar waveguide: Quantifying the coupling strength,” *Phys. Rev. Applied* **14**, 054060 (2020).
- [30] D. Vanmaekelbergh and L. K. van Vugt, “ZnO nanowire lasers,” *Nanoscale* **3**, 2783–2800 (2011).
- [31] M. A. M. Versteegh, D. Vanmaekelbergh, and J. I. Dijkhuis, “Room-Temperature Laser Emission of ZnO Nanowires Explained by Many-Body Theory,” *Phys. Rev. Lett.* **108**, 157402– (2012).
- [32] B. W. Hakki and T. L. Paoli, “Gain spectra in GaAs double - heterostructure injection lasers,” *J. Appl. Phys.* **46**, 1299–1306 (1975).
- [33] P. Blood, G.M. Lewis, P.M. Snowton, H. Summers, J. Thomson, and J. Lutti, “Characterization of semiconductor laser gain media by the segmented contact method,” *IEEE Journal of Selected Topics in Quantum Electronics* **9**, 1275–1282 (2003).
- [34] K. L. Shaklee and R. F. Leheny, “Direct determination of optical gain in semiconductor crystals,” *Applied Physics Letters* **18**, 475–477 (1971), <https://doi.org/10.1063/1.1653501>.
- [35] D. Solnyshkov, H. Ouerdane, and G. Malpuech, “Kinetic phase diagrams of gan-based polariton lasers,” *Journal of Applied Physics* **103**, 016101 (2008), <https://doi.org/10.1063/1.2822148>.
- [36] E. Rosencher and B. Vinter, *Optoelectronics* (Cambridge University Press, 1998).
- [37] G. Mohs, T. Aoki, R. Shimano, M. Kuwata-Gonokami, and S. Nakamura, “On the gain mechanism in gan based laser diodes,” *Solid State Communications* **108**, 105–109 (1998).
- [38] M. Leroux, N. Grandjean, B. Beaumont, G. Nataf, F. Semond, J. Massies, and P. Gibart, “Temperature quenching of photoluminescence intensities in undoped and doped GaN,” *Journal of Applied Physics* **86**, 3721–3728 (1999), <https://doi.org/10.1063/1.371242>.